

TURBULENCE MODELING TREATMENT FOR ROTORCRAFT WAKES

Mark Potsdam
Aeroflightdynamics Directorate
US Army Research, Development, and Engineering Command
Moffett Field, CA 94035
mpotsdam@mail.arc.nasa.gov

Thomas Pulliam
NASA Ames Research Center
Moffett Field, CA 94035
tpulliam@mail.arc.nasa.gov

ABSTRACT

This work investigates the influence of turbulence modeling in the vortical wake of rotorcraft simulations. It is seen that for a range of flight conditions, but especially hover, overall rotor performance prediction can be significantly affected by the wake turbulence model characteristics. The characteristics of some baseline turbulence model formulations (e.g. Baldwin-Barth, Spalart-Allmaras) are observed to produce too much turbulent eddy viscosity if the production is based on the vorticity field of the vortex-dominated rotor wake. Due to the excess production of the turbulent eddy viscosity in the wake, and its subsequent convection and diffusion, the wall-bounded viscous flow is modified. To ameliorate these difficulties, turbulence model modifications in the wake, such as turning off the production source terms, are evaluated. They are shown to improve solution accuracy compared with experimental data for a quarter-scale V-22 isolated rotor in hover, a CH-47 isolated rotor in hover, and a UH-60A in forward flight at high thrust coefficient. The overall effect on rotor performance can be several points in rotor figure of merit or a variation in stall boundary thrust coefficient.

INTRODUCTION

Unlike fixed wing aerospace vehicles, the wake of a rotorcraft has a significant effect on the overall flow field and, more importantly, on the performance of the vehicle. A rotorcraft in hover and edgewise flight is flying in its own wake. The wake is characterized by induced velocities and regions of intense vortical flow which interact with rotor blades, fuselages, and empennages. These interactions can adversely affect the rotorcraft performance, noise, and vibration characteristics. In computational fluid dynamics (CFD) analyses of rotorcraft it is desired to model the rotor and tip vortices as accurately as possible. Techniques which have frequently been applied include high-order schemes, adaptive mesh refinement, multidisciplinary coupling, and viscous flow with advanced turbulence modeling [1,2].

Turbulence modeling for rotorcraft is important for both rotor and fuselage analyses as well as the wake. Rotorcraft fuselages, due to operational constraints, are rarely streamlined

bodies and contain bluff body separation on pylons and ramps. Rotor blades at high speed and/or high thrust conditions may enter dynamic stall on the retreating side and shock/boundary layer separation on the advancing side. Turbulence modeling also plays a role in resolving the details of the tip vortices. Therefore, the turbulence model behavior has an effect on both the near- and far-field flow.

The main objective of this work is the application of state-of-the-art engineering turbulence models, such as the Spalart-Allmaras model, to practical rotorcraft problems. The aim, which is important to the rotorcraft community, is to determine their overall effectiveness and accuracy along with details of how their implementation affects rotor performance prediction in hover and forward flight. It will be seen that the typical dependence in many turbulence models of the eddy viscosity production term on vorticity is problematic for highly vortical flows such as rotorcraft wakes. Modifications to the production term, such as turning it off or the Dacles-Mariani correction, are utilized. The purpose of this paper is not to discuss the details of turbulence modeling and especially not turbulence model development. Nor is the goal to investigate turbulence modeling in accurately capturing the details of the viscous flow within the wake tip vortices.

Presented at the AHS Specialist's Conference on Aeromechanics, San Francisco, CA, Jan. 23-25, 2008. Copyright 2008 by the American Helicopter Society International, Inc. All rights reserved.

This paper is organized as follows. First a brief background on turbulence modeling as it relates to vortical flows is presented. Then, the overset grid methodology using the CFD flow solver OVERFLOW-2 is described. Three different rotorcraft test cases (quarter-scale V-22, CH-47, and UH-60) are investigated in hover and forward flight to determine the effect of off-body turbulence model treatment. Finally, conclusions are presented.

BACKGROUND

The Reynolds-averaged Navier-Stokes (RANS) equations require a turbulence closure model for the turbulent Reynolds stresses. A common solution has been to adopt the Boussinesq approximation, which makes use of the turbulent eddy viscosity (μ_t) concept. Within the aerospace community the one-equation Spalart-Allmaras (SA) model [3] and variants of the two-equation $k-\omega$ turbulence model [4], including Menter SST [5], have seen wide use for engineering applications of external flow prediction over airfoils, wings, and rotors. In the past, the one-equation Baldwin-Barth (BB) model [6] has been used, but due to reduced accuracy and freestream sensitivity has now mostly been abandoned in favor of the SA model [4]. It still finds some use in various applications due to the lower values of turbulent eddy viscosity generated in separated regions away from walls [7]. Other two- and higher- equation models are currently in use, but none in particular have yet to gain widespread engineering acceptance, for example v^2-f [8], KES [9], and Reynolds Stress Transport models [4]. Detached Eddy Simulation (DES) models, wherein a RANS model is used for wall-bounded flow and large eddy simulation (LES) is employed away from the wall, is currently receiving significant research attention and has shown good results for flows with massive separation [10].

The SA model is written as [3]:

$$\begin{aligned} \frac{\partial \tilde{\nu}}{\partial t} + U_j \frac{\partial \tilde{\nu}}{\partial x_j} &= c_{b1} [1 - f_{t2}] \tilde{S} \tilde{\nu} - \\ &\left[c_{w1} f_w - \frac{c_{b1}}{\kappa^2} f_{t2} \right] \left(\frac{\tilde{\nu}}{d} \right)^2 + \\ &\frac{1}{\sigma} \frac{\partial}{\partial x_k} \left[(\nu + \tilde{\nu}) \frac{\partial \tilde{\nu}}{\partial x_k} \right] + \frac{c_{b2}}{\sigma} \frac{\partial \tilde{\nu}}{\partial x_k} \frac{\partial \tilde{\nu}}{\partial x_k} \end{aligned} \quad (1)$$

where c_{b1} , c_{w1} , c_{b2} , κ , and σ are constants, $\tilde{\nu}$ is the modified eddy viscosity, and U is the velocity. The terms on the left-hand side are the unsteady and convection terms. On the right-hand side are the production, destruction, dissipation, and diffusion. Of interest here is the modeling of the velocity gradient term in the production source [11]:

$$\tilde{S} = f_{v3} S + \frac{\tilde{\nu}}{\kappa^2 d^2} f_{v2} \quad (2)$$

where d is the distance to the closest surface. In Eqns. 1 and 2, the f are complex functions. S is prescribed as the vorticity magnitude, which makes the turbulent eddy viscosity production directly dependent on the vorticity.

The production term in the Baldwin-Barth model is also based on the vorticity. Various forms of the $k-\omega$ two-equation model use vorticity and/or strain in their formulations. The substitution of vorticity for strain has been used to reduce problems around stagnation points and regions of inviscid flow [12]. However, with proper limiting it is possible to develop models which only use strain [13]. Note that in wall-bounded flows the strain and vorticity are of similar magnitude, which makes the substitution reasonable. This is not true in a vortex core where the vorticity is high, but the strain is low. In theory the turbulence modeling production term is based on a velocity gradient [4].

The dependence of the production term on vorticity is problematic. The eddy viscosity can be drastically over-produced in the vortex core with these models, whereas it would normally be suppressed by the stabilizing effects of rotation [14,15]. Existing turbulence models and modifications have been proposed to include the effects of rotation and account for this non-physical dependence:

1. Turbulence models which explicitly include rotation and curvature terms do not suffer from this problem. This includes the full Reynolds Stress turbulence models (RSM). They are, however, still quite expensive, not robust enough for engineering application, and yet to fully show improved accuracy [16].

2. Rotation and curvature corrections have been developed for application to a range of turbulence models. Spalart [16] proposes an empirical alteration to account for rotation and curvature by introducing additional Galilean-invariant, higher derivative terms. Duraisamy [8] modified Durbin's v^2-f model to include streamline curvature effects as a Galilean-invariant correction to the eddy viscosity sensitized to strain and vorticity. There are numerous others.

3. A simpler correction has been proposed by Dacles-Mariani [14] and was originally implemented for the production term, P , of the Baldwin-Barth model:

$$P = c_l \nu R_t S \quad (3)$$

where c_l is a constant, ν is the laminar viscosity, R_t is the turbulent Reynolds number, and S is a scalar measure of the deformation tensor. S can be based on vorticity magnitude, $|\omega|$, as in the SA model, the strain rate, $|s|$, or a combination of the two. The Dacles-Mariani (DM) corrected form is:

$$P = c_1 \nu R_t (|\omega| + c_{prod} \min(0, |s| - |\omega|))$$

$$|s| = \sqrt{2S_{ij}S_{ij}}, \quad S_{ij} = \frac{1}{2} \left(\frac{\partial u_j}{\partial x_i} + \frac{\partial u_i}{\partial x_j} \right) \quad (4)$$

$$|\omega| = \sqrt{2\Omega_{ij}\Omega_{ij}}, \quad \Omega_{ij} = \frac{1}{2} \left(\frac{\partial u_j}{\partial x_i} - \frac{\partial u_i}{\partial x_j} \right)$$

where c_{prod} is a constant usually set to 2.0. It can be seen that in regions of high vorticity, where the vorticity exceeds the strain, such as a tip vortex, the production is reduced or becomes negative (destruction). In regions where strain and vorticity are of similar magnitude, such as boundary and shear layers, there is no affect as the correction term goes to zero. A similar modification can be made in the SA source term, Eqn. 2 [17].

4. A simple alternative is to turn off the production terms in the off-body grid wake region. This is typically only possible in multiblock or overset mesh systems, although a distance function could theoretically be implemented for unstructured meshes. In this work, this implementation is termed a “laminar off-body” assumption in that the turbulence that is generated elsewhere can still convect, dissipate, and diffuse, but it cannot be produced. The modification has some physical basis, as experimental studies on wing tip vortices have found reduced turbulence levels and analytical studies indicate laminar diffusion mechanisms due to the solid body rotation in the vortex core [8].

5. An even simpler ad hoc modification includes completely turning off the turbulence model in the wake such that the eddy viscosity remains at its freestream value. The freestream value of eddy viscosity sets the boundary condition to any near-body grid blocks where the turbulence model is activated.

Proper treatment of the turbulence in the vortical wake can be important whether or not the tip vortex is fully resolved. It is estimated that 10 to 20 points, depending on the accuracy of the numerical scheme, are required to accurately resolve the vortex core [14,15]. General, robust methods for tracking the vortex core are still under development. Therefore, a common gridding approach is to use uniform Cartesian grids in the rotorcraft wake. With this approach, it is estimated that well over 1 billion grid points are required to uniformly capture the wake – based on a rotor aspect ratio of 15, a tip vortex size of 10% of the rotor tip chord, and approximately 10 points across the core, all resulting in a uniform grid spacing of 1% of the blade chord. Current practical calculations with uniform Cartesian off-body grids [e.g. 18,19] typically use grid spacing of 5-10% of the chord, resulting in 10-50 million grid points for an isolated rotor. In this case, the vortices will be under-resolved and over-dissipated. However, these

calculations still represent state-of-the-art engineering computations.

METHODOLOGY

CFD calculations use the Reynolds-averaged Navier-Stokes computational fluid dynamics code OVERFLOW-2.0/2.1 [20,21]. The code is continually being developed at NASA and has been applied to a wide range of fluid dynamics problems. OVERFLOW-2 includes capability, integrated from OVERFLOW-D [22], for time-dependent dynamic rigid body motion of components. Solutions are computed on structured, overset grids using body-conforming “near-body” grids and automatically generated Cartesian “off-body” grids in the wake and farfield. The off-body grids are generated by level with grid spacing increased by a factor of two at each level until reaching the outer boundary of the computational domain.

Several modifications to the code for calculations of hovering rotors have been made [18,23]. In particular, isolated rotor flows can be computed as steady-state problems in a blade-fixed reference frame with the addition of a rotational source term. The steady-state formulation may offer some efficiency advantages over a time-accurate moving blade simulation. A modified source/sink boundary condition is implemented for hover. Both the steady and conventional moving grid unsteady formulations are used here and compared.

User-generated XML inputs files prescribe the arbitrary six degree-of-freedom forced motion. Information between the various overlapping grids (domain connectivity) is exchanged through interpolations at the inter-grid boundaries. Relative grid motion necessitates recalculation of the domain connectivity, including hole cuts and interpolation coefficients, at each time step as the near-body grids move through the stationary off-body Cartesian grids.

Spatial decomposition for parallel processing is achieved by distributing grids among the processors, and, if necessary, splitting them as appropriate into smaller blocks for load balancing. Boundaries that are created in the splitting process have explicit boundary conditions, similar to intergrid boundaries of the original overset grid system. This grid splitting methodology has implications for turbulence modeling of wall-bounded flows when the grid is subdivided in the wall normal direction. Care must be taken to pre-calculate the wall distance function before grid splitting.

OVERFLOW includes a wide range of options for numerical methods, boundary conditions, and turbulence models. Throughout this work, except as noted, fourth-order central spatial differencing with second- and fourth difference scalar artificial dissipation is used for the

convective terms in both the near- and off-body grids. Steady-state calculations use a scalar pentadiagonal Pulliam-Chaussee algorithm with a variable time step. Time-accurate simulations make use of a dual-time stepping scheme for second-order temporal accuracy.

Viscous modeling is used in the curvilinear near-body grids along with a turbulence model. For the uniform Cartesian off-body grids, the viscous terms are not included (inviscid assumption) since the grid-related dissipation is already much larger than any viscous dissipation that might be present in the solution. This is attributable to the large grid spacings used relative to an actual vortex core size. However, the crux of the investigations in this paper is that despite the absence of the viscous terms, the treatment of the turbulence model in the wake, especially in an overset grid context, can have a significant impact on the near-body viscous solution. In the rotorcraft applications that follow, modification items 3 (Dacles-Mariani), 4 (production terms – laminar off-body), and 5 (freestream eddy viscosity) from the Background section are investigated.

QUARTER-SCALE V-22 (TRAM) HOVER

The Tilt Rotor Aeroacoustics Model (TRAM) is a wind tunnel model constructed to facilitate tiltrotor aeromechanics research. The geometry is a 0.25-scale V-22 nacelle and 3-bladed rotor with geometric and dynamic scaling. The isolated TRAM rotor was tested in the Duits-Nederlandse Windtunnel Large Low-speed Facility (DNW-LLF) in the spring of 1998. It provides a significant source of aeroacoustics, performance, and structural loads data for validation of tiltrotor analyses. Among the aerodynamics data acquired were rotor performance and blade pressures. Hover runs were performed at nominal tip Mach numbers of 0.58 and 0.62, rather than the V-22 hover tip Mach number of 0.72. Details of the test and data reduction are described in Refs. 24 and 25.

The main physical characteristics of the quarter-scale V-22 rotor are presented in Table 1, and nominal test parameters in hover are summarized in Table 2. The TRAM rotor is similar to the V-22 except that the blade root fairings are modified. The large amount of nonlinear twist as well as thick inboard airfoils are typical of tiltrotors but significantly different from helicopter rotor configurations. Details of the models and geometries have been described in Ref. 26.

The 3-bladed TRAM rotor is shown in Figure 1. Elastic blade effects are not modeled. The centerbody is a V-22 spinner with a faired boattail and is used to prevent recirculation of the blade root vortices. The blade hub is modeled without connecting flexbeams and is physically separated from the spinner.

In the Chimera methodology, overset, structured near-body grids are generated about the geometry. They extend approximately one tip chord (c_{tip}) away from the body and include sufficient resolution to capture boundary layer viscous effects. The baseline surface grids for the V-22 configurations are also shown in Figure 1. They use C-mesh topology blades and tip caps. Grid spacing parameters are described in Ref. 18.

Off-body Cartesian grid generation is automatically performed by OVERFLOW. The finest off-body spacing for the baseline grid is $0.10c_{tip}$. This level-1 grid surrounds the blades and extends $\pm 1.23R$ in x and y and $-0.58R, +0.23R$ in z . A total of five progressively coarser levels are generated out to the farfield boundary, which is placed at $5R$ in all directions from the center of the domain. The grid contains 15.9 million (M) points: 6.2M near-body and 9.7M off-body. Where grid points fall inside the geometry, hole cutting is employed to blank out these points. A cut through the grid system in Figure 2 shows the near- and off-body grids, hole cuts, and overlap.

Significant CFD validation with this dataset has previously been performed using OVERFLOW-D [18] for both steady and unsteady isolated hover as well as installed configurations. Some calculations on this configuration in this paper use the Baldwin-Barth turbulence model. At the time it was the only one-equation model available in OVERFLOW-D, whose results are useful for comparison.

Calculations for the TRAM rotor are focused on a 14-degree collective case (thrust coefficient, $C_T \sim 0.015$). TRAM performance prediction using the various wake turbulence modeling options are shown in Table 3. For the steady-state calculations using the baseline Baldwin-Barth model in the near- and off-body grids the figure of merit (FM) is 0.728. By turning off the production source terms (laminar off-body) or setting freestream turbulent viscosity in the off-body grids, the FM is increased to 0.749 and 0.752, respectively, which brings it in better agreement with the test data, 0.780. One hundredth (0.01) in FM is typically the desired accuracy for hover calculations and, for the dual-rotor V-22, can account for a 380 lbs. change in useful load. While both turbulence model modifications show similar improvements, the laminar off-body assumption is more physically plausible as it does not abnormally truncate the eddy viscosity in the grid overlap regions. The freestream μ_T implementation has implications when moving, oversets grids are used in that care should be taken to continually zero out the values of μ_T that are passed to the near-body intergrid boundary points. Based on results from Ref. 18, it is expected that the fully turbulent computational results may under-predict the experimental figure of merit by as much as 0.014 due to laminar boundary

layer transition effects. Therefore, overall performance results are still slightly underpredicted.

Figure 3 shows details of the turbulent eddy viscosity in the wake for the baseline and laminar off-body models. A centerline wake cut (30-deg wake age) is shown with vorticity on the left and μ_T on the right. Figure 4 shows μ_T contours of the wall-bounded flow at 90% span. The over-production of turbulence for the baseline model is dramatically clear in these figures. It must be noted that the scales on the figures are different by at least an order of magnitude ($\mu_{Tmax} = 16900$ for the baseline model, and $\mu_{Tmax} = 2450$ for the laminar off-body model). In the view of the wall bounded flow, the differences are due to the over-production of eddy viscosity and resulting convection from the wake. As seen in the relative velocity magnitude contours at 90% span in Figure 5, the boundary layer of the baseline model is thicker due to the excess eddy viscosity, and this affects the overall rotor performance.

Figure 6 shows the thrust and torque spanwise loadings for the two solutions. It is seen that the thrust loadings are very similar, but there is increased torque on the outboard of the rotor due to the modified boundary layer profiles in the baseline solution. This figure indicates that the performance differences are due to viscous (profile) drag and not inflow (induced) effects. Figure 3 also indicated that the wake vorticity is almost completely unchanged as are the inflow velocities (not shown).

Table 3 also shows calculations using the Spalart-Allmaras turbulence model. It is not as sensitive to the off-body turbulence treatment as BB for this geometry configuration and flow conditions. The laminar off-body and Dacles-Mariani (DM) correction both give a FM of 0.757, which is only 0.004 higher than the baseline SA model. All are in good agreement with the modified BB results. Unfortunately, it was not possible to obtain results with the Menter SST models in OVERFLOW 2.0 or 2.1 due to start-up stability difficulties. It would have been useful to compare the vorticity- and strain-based formulations which are available.

Figure 7 shows residual convergence for the blade, root, and tip near-body grids, and the level-1 off-body grid for the BB laminar off-body solution. The characteristics for all grids are excellent, and the residuals continue to reduce without stalling out, even after 80,000 iterations. This high level of convergence has not typically been seen in steady-state hover calculations. The turbulence model residual convergence (not shown) is equally well behaved for all grids. With the baseline BB model, however, the turbulence model residual convergence in the tip cap grid is poor. Figure 8 shows the corresponding figure of merit history. In spite of the steady, uniform convergence rate, the

overall forces and moments are, nonetheless, relatively slow to converge, although 80,000 iterations are not required.

For comparison with the steady-state results, unsteady calculations were also performed. Dual-time stepping with 0.56 deg per time step (640 steps per revolution) and 10 subiterations was used. A 1.6 and 2.5 drop in the right-hand side subiteration residual was obtained for the blade and level-1 off-body grid, respectively. Increasing the number of subiterations to 20 increased the FM for the SA laminar off-body unsteady case by only 0.0017. Solutions were run out for at least 6 rotor revolutions for BB and 13 revolutions for SA. In both cases (SA and BB) there exists a discrepancy between performance predictions in state-state and unsteady modes. This discrepancy was noted in Ref. 18 and has not been resolved. It does not appear that the 2nd-order temporal accuracy over the 1st-order time stepping in OVERFLOW-D has remedied the problem. Unlike Ref. 18, results here indicate that the unsteady formulation gives higher figures of merit and better agreement with test data.

The FM values for the unsteady calculations are also indicated in Table 3. Unsteady BB laminar off-body results are within 0.018 of the experimental data. Unsteady SA turbulence model variants are essentially the same and within 0.007 of the test data. Both models are approximately 0.014 higher than the corresponding steady-state results. Unsteady SA-DES results indicate no improvement over the SA unsteady RANS results. Note that it has also been found that the DES model in and of itself does not include the correct rotational flow behavior, and some correction may still be needed for certain flows [17].

There is a noticeable but not excessive efficiency penalty, less than a factor of 2, associated with the unsteady TRAM simulation compared with the steady formulation. The steady-state solution is force/moment converged after 40,000 iterations while the unsteady simulations cost an equivalent 38,400-83,200 iterations. A larger number of subiterations for tighter inner iteration convergence adversely affects the cost comparison.

CH-47 HOVER

The CH-47D Chinook is a multi-mission transport helicopter. Full-scale whirl tower testing of the isolated CH-47 rotor was performed in 1978 on the Boeing Whirl Tower Test Stand. Numerous test data were taken, including rotor blade tracking, stress and motion (loads measurement), rotor blade natural frequency determination, blade performance evaluation and endurance testing. Details of the rotor configuration are given in Table 1 while nominal, non-proprietary hover test parameters are shown in Table 2. The data used for comparison are non-dimensionalized and presented relative to the

experimental values. Significant computational hover analyses of the isolated rotor and installed dual-rotor configuration were performed in Ref. 19.

The computational model for the rotor was derived from Boeing CAD data. Each blade of the 3-bladed rotor has 3 body-fitted O-meshes as shown in Figure 9. The off-body Cartesian grid components are comprised of 9 automatically generated levels and extend 15.4 rotor radii from the rotor center. The grid spacing on the finest Cartesian grids is equal to 0.06 blade chord lengths in the regions surrounding the rotor, centerbody, and near wake. This small grid spacing, however, still does not allow for accurate capturing of the tip vortices. The complete grid system is comprised of approximately 35 million grid points. Compared with the tiltrotor blade, these helicopter blades are quite flexible, however, no aeroelastic effects have been included here except for coning (5.5 deg). This will have some effect on the absolute performance prediction.

Time-accurate solutions were computed using both the baseline and laminar off-body versions of the Spalart-Allmaras turbulence model. An equivalent time step of 0.25 deg with 16 dual-time subiterations was used. The baseline solutions are taken from Ref. 19 and use a 2nd-order central difference scheme in the near-body grids. Laminar off-body solutions in this work use a 4th-order scheme in the near-body grids. They were run for 12-14 rotor revolutions, when the thrust and torque finally reached a steady state. The CH-47 isolated rotor solutions are slow to reach a converged state, and forces and moments do not converge smoothly. The baseline solutions, in particular, show very poor figure of merit convergence due to the turbulence model characteristics.

Table 4 compares the computational figure of merit against the test data for a range of collective angles: 8 – 12 deg. The thrust values for the three computational data points span the design thrust for the CH-47 rotor plus or minus about 7500 pounds. The laminar off-body assumption, along with the 4th-order near-body scheme, results in a significant improvement in performance prediction for this rotor – upwards of a 0.06 increase in FM. The FM agreement with the experimental test data is within 0.007. The steady-state result in Table 4 is inexplicably low compared with the equivalent unsteady simulation.

Figure 10 shows the CH-47 isolated rotor wake geometry (Q criteria) and surface pressures in hover. Figure 11 shows eddy viscosity contours for the baseline and laminar off-body solutions. Noting the large difference in μ_T scales, there is significantly higher turbulence production in the baseline model due to the wake vorticity, which itself is relatively unchanged between solutions.

The SA turbulence model trends on the CH-47 are somewhat different from the TRAM

rotor, where SA versions showed little effect. The full-scale CH-47 rotor differs from the quarter-scale V-22 configuration (with reduced tip speed) in that the CH-47 disk loading (T/A) is almost half. The lower disk loading results in slower convection of the wake downward ($v_h = \sqrt{T/2\rho A}$), and most likely allows for more interaction of the wake turbulence with the wall-bounded viscous flows.

UH-60A FORWARD FLIGHT

A unique and extensive flight test database exists for a UH-60A Blackhawk helicopter in level flight and transient maneuvers [27,28]. The data were obtained during the NASA/Army UH-60A Airloads Program. The database provides aerodynamic pressures, structural loads, control positions, and rotor forces and moments, allowing for the validation of both aerodynamic and structural models. The test matrix contains a range of advance ratios and gross weight coefficients (Figure 12).

The UH-60A master input database has been used to define the elastic UH-60A 4-bladed rotor. The database contains geometric, aerodynamic, and structural material properties. Details of the rotor configuration are given in Table 1. A theoretical UH-60A CFD blade grid was developed using definitions of the SC1095 and SC1094R8 airfoils combined with twist, chord, quarter chord location, and trim tab distributions. Realistic tip cap and root definition have also been used. The blunt trailing edge airfoils are closed for ease of grid generation.

For each of the 4 blades, 3 near-body grids define the blade, root cap, and tip cap. They extend about one chord away from the surface and include sufficient resolution to capture boundary layer viscous effects. Blade and cap grids use a C-mesh topology to better capture the shear layer from the blades. Grid generation details are available in Ref. 29. The blade and tip cap surface grids are shown in Figure 13. The finest off-body spacing for the baseline grid is 0.10 chords. This level-1 grid surrounds the blades and extends $\pm 1.2R$ in x and y and $\pm 0.3R$ in z. A total of five progressively coarser levels are generated out to the farfield boundary, which is placed at 5R in all directions from the center of the domain. The baseline grid contains 26.1 million (M) points: 14.4M near-body (55%) and 11.7M off-body (45%). A coarse grid with every other point extracted from the baseline grid is also used in this work. Where grid points of overset meshes fall inside the geometry, hole cutting is employed to blank out these points. A cut through the grid system in Figure 13 shows the deflected near-body grids (blue) and level-1 (red) Cartesian off-body grids, hole cuts, and grid overlap. An azimuthal step size of 0.05 degrees is used in all CFD calculations, corresponding to 1800 iterations per 90 degrees of rotation of the 4-bladed rotor.

The OVERFLOW-2 runs use 2nd-order spatial central differencing and an implicit 1st-order temporal scheme in the near-body grids. The Baldwin-Barth one-equation turbulence model is employed in the near-body grids, which are assumed fully turbulent. These algorithmic choices match those used previously with OVERFLOW-D.

Flight counter c9017 is an intermediate speed, 0.24 advance ratio, high thrust coefficient, level flight test point flown at 17,000 ft. The freestream Mach number is 0.157. The test point is detailed in Table 2. This is a challenging and quintessential rotorcraft test case due to the wide variation of unsteady flow conditions, ranging from transonic to dynamic stall, with noticeable wake interactions. The dynamic stall characteristics of this test point have previously been discussed in detail [30] as well as investigated computationally [29,31]. The c9017 test point lies on the stall boundary of the UH-60A as indicated in Figure 12. This turns out to be an important consideration in the simulation of this case as it indicates that it may, in fact, not be possible to trim the helicopter to these conditions due to small modeling details.

Previous calculations [29] using a CFD/CSD coupled aeroelastic methodology (OVERFLOW-D/CAMRAD II [26]) obtained good agreement with measured airloads. The Baldwin-Barth turbulence model with freestream μ_T in the off-body grids was used. OVERFLOW-D/CAMRAD II were able to trim to the desired flight conditions ($C_T/\sigma = 0.129$), and periodic aeroelastic blade motions were obtained from the CFD/CSD coupling. The resulting collective control was 14.0 deg.

With the upgrade to OVERFLOW-2 in the coupling methodology, it was no longer possible to trim to the desired thrust target. The off-body turbulence modeling treatment played a major role. Figure 14 shows normal force and pitching moment at 86.5% span for OVERFLOW-2 with the baseline Baldwin-Barth, laminar off-body, and freestream μ_T variants. The aeroelastic rotor motions are those obtained from the OVERFLOW-D/CAMRAD coupling. It is seen that for this forward flight case the baseline and laminar off-body BB results are quite similar but that the freestream μ_T results have a slightly delayed stall near 250 deg azimuth and match the original OVERFLOW-D calculations. Unlike hover conditions, the convection speed for the transport of μ_T is relatively large, and the laminar off-body assumption has little effect.

The small stall delay allows the freestream μ_T solution to trim to the desired thrust conditions. With the baseline or laminar off-body turbulence model implementations, it is found that the rotor cannot achieve the desired thrust. Figure 15 shows a collective sweep, using the coupled CFD/CSD methodology (with CAMRAD II) with baseline BB and freestream μ_T . With freestream μ_T , the trim target is obtained at a collective of 14.1 deg (12.9

root pitch), and higher thrust values are achieved at increased collective angles. On the other hand, the analysis using the baseline BB model shows a stalled out rotor that never reaches the desired trim target but only approaches it at 17 deg collective. Note that the measured flight test main rotor root pitch for c9017 is approximately 11 deg, which is in reasonable agreement with the 12.9 deg root pitch and is much lower than the corresponding 17 deg collective would indicate.

Figure 16 shows μ_T iso-surfaces on the UH-60A in forward flight for this dynamic stall case. The flow is from left to right. The baseline model (a) highlights the stall on the rotor as well as turbulence production in the tip and supervortices. The laminar off-body result (b) shows turbulence only in the near-body stall region. The freestream μ_T result (c) shows a significant amount of eddy viscosity throughout the stalled region of the rotor in the 3rd and 4th quadrants. However, this representation is not physically realistic due to an incorrect implementation of the turbulent boundary condition exchange with moving grids. Most of the turbulence in this case was deposited in the off-body grids as intergrid boundary conditions while the blades were passing through. With no turbulence model activated, the deposited turbulence cannot dissipate or convect away from the rotor with the freestream. This artificially results in excessive freestream turbulence seen by the rotor, resulting in delayed blade stall. The faulty freestream μ_T result serves to point out the effect that extraneous or excessive turbulent eddy viscosity might have in stall prediction. If the wake of one rotor convects into and interferes with a downstream fuselage, empennage, or second rotor (e.g. CH-47D), the downstream flow could be similarly affected in forward flight.

It is also not possible to obtain a trimmed solution on the coarse grid using the baseline SA model. However, the SA model on the baseline grid does obtain a trimmed solution to the c9017 flight conditions, further indicating the sensitivity of this edge-of-the-envelope calculation to CFD and turbulence modeling variations. OVERFLOW-2/CAMRAD II baseline grid SA results are compared against OVERFLOW-D/CAMRAD II baseline grid BB results along with flight test data in Figure 17. The two CFD results are in reasonable agreement, although the SA model with OVERFLOW-2 does predict more stall.

For the c9017 flight conditions which are near the thrust boundary of the rotor, it is seen that CFD and turbulence modeling details have an effect not only on the solution, but also on whether a trimmed solution can even be obtained. The margin of error in Figure 15 is less than 1% of thrust. It is doubtful that the test data is accurate to this level given uncertainties in airloads measurements, fuselage download, and empennage lift. Known

sensitivities of CFD stall prediction to turbulence modeling [1], grid effects [29], and elastic motions [31] have an influence on the details and overall viability of the solution. Details of the force integration between CFD and CSD, such as neglecting the tip caps, can also attribute to discrepancies of this magnitude.

CONCLUSIONS

This work has examined turbulence modeling in the rotorcraft wake and specifically its effect on rotor performance prediction. The following conclusions are made:

1. Even when the vortical rotorcraft wake is under-resolved and/or inviscid, the turbulence model treatment in the off-body flowfield can have a significant effect on the wall-bounded flow, and, therefore, the rotor performance prediction.
2. Turbulence models that are incorrectly sensitized to vorticity will, in general, perform poorly, resulting in excessive turbulence production in the vortical rotorcraft wake.
3. Turbulence model modifications to remove this sensitivity are recommended. Modifications include turning off production terms ("laminar off-body"), strain/vorticity substitutions (Dacles-Mariani correction), and/or rotation and curvature corrections (not investigated here).
4. Results on two isolated rotor configurations in hover (quarter-scale V-22 and CH-47) show better agreement with experimental hover performance data (figure of merit) when the turbulence models are correctly sensitized for vortical flows. In forward flight at high thrust coefficient (UH-60A), the turbulence model treatment was seen to affect the stall boundary prediction. However, trends are somewhat configuration and turbulence model dependent.
5. Discrepancies exist between isolated hover performance predictions using steady-state and moving grid, unsteady formulations. In OVERFLOW-2, the unsteady formulation currently gives better accuracy in comparison with test data on a tiltrotor (V-22) and helicopter rotor (CH-47) configuration. The cause of the difference is not known.
6. When trimming to flight conditions known to be near the rotor stall boundary, there is an understandable possibility that the trim target is not achievable. Alternate trim conditions, such as fixed collective, may be necessary to approach the desired conditions. Edge-of-the-envelope solutions are known to be sensitive to various numerical modeling issues, including but not limited to the near- and off-body turbulence model treatment.

ACKNOWLEDGEMENTS

The authors gratefully acknowledge the use of the computer facilities at the NASA Advanced Supercomputing (NAS) Division and the Dept. of Defense NAVO Major Shared Resource Center (MSRC). Arsenio Dimanlig of the Eloret Corp. provided helpful assistance with the CH-47D calculations. Use of the CH-47D experimental data, courtesy of The Boeing Co., is appreciated. Thomas Olsen of the Eloret Corp. performed the UH-60A baseline grid coupled simulation.

REFERENCES

1. Duque, E. P. N., Sankar, L. N., Menon, S., Bauchau, O., Ruffin, S., Smith, M., Ahuja, K., Brentner, K. S., Long, L. N., Morris, P. J., and Gandhi, F., "Revolutionary Physics-Based Design Tools for Quiet Helicopters," AIAA 2006-1068, AIAA 44th Aerospace Sciences Meeting and Exhibit, Reno, NV, January 2006.
2. Datta, A., Nixon, M., and Chopra, I., "Review of Rotor Loads Prediction with the Emergence of Rotorcraft CFD," *Journal of the American Helicopter Society*, Vol. 52, No. 4, October 2007, pp. 287-317.
3. Spalart, P. R., and Allmaras, S. R., "A One-Equation Turbulence Model for Aerodynamic Flows," AIAA 92-0439, AIAA 30th Aerospace Sciences Meeting and Exhibit, Reno, NV, January 1992.
4. Wilcox, D. C., "Turbulence Modeling for CFD," ISBN 1-928729-10-X, 2nd Ed., DCW Industries, Inc., 2004.
5. Menter, F. R., "Two-Equation Eddy-Viscosity Turbulence Models for Engineering Applications," *AIAA Journal*, Vol. 32, No. 8, 1994, pp. 598-605.
6. Baldwin, B. S., and Barth, T. J., "A One-Equation Turbulence Transport Model for High Reynolds Number Wall-Bounded Flows," AIAA 91-0610, AIAA 29th Aerospace Sciences Meeting and Exhibit, Reno, NV, January 1991.
7. Buning, P. G., "Simulation of Capsule Pitch Damping Aerodynamics Using CFD," 8th Symposium on Overset Composite Grid and Solution Technology, Houston, TX, October 2006. <http://www.arl.hpc.mil/events/Overset2006/program.html>

8. Duraisamy, K., and Iaccarino, G., "Curvature Correction and Application of the v^2 - f Turbulence Model to Tip Vortex Flows," Center for Turbulence Research, Stanford University, Annual Research Briefs, 2005. <http://www.stanford.edu/group/ctr/ResBriefs/temp05/duraisamy.pdf>.
9. Shelton, A. B., Braman, K., Smith, M. J., and Menon, S., "Improved Turbulence Modeling for Rotorcraft," American Helicopter Society 62nd Annual Forum, Phoenix, AZ, May 2006.
10. Strelets, M., "Detached Eddy Simulation of Massively Separated Flows," AIAA 2001-0879, AIAA 39th Aerospace Sciences Meeting and Exhibit, Reno, NV, January 2001.
11. Lee-Rausch, E. M., Buning, P. G., Mavriplis, D., Morrison, J. H., Park, M. A., Rivers, S. M., and Rumsey, C. L., Sensitivity Analysis of a Drag Prediction Workshop Wing/Body Transport Configuration," AIAA 2003-3400, AIAA 21st Applied Aerodynamics Conference, Orlando, FL, June 2003.
12. Menter, F. R., "Improved Two-Equation k - ω Turbulence Models for Aerodynamic Flows," NASA TM 103975, October 1992.
13. Nichols, R., Tramel, R., and Buning, P., "Solver and Turbulence Model Upgrades to OVERFLOW 2 for Unsteady and High-Speed Applications," AIAA 2006-2824, AIAA 24th Applied Aerodynamics Conference, San Francisco, CA, June 2006.
14. Dacles-Mariani, J., Zilliac, G., Chow, J., and Bradshaw, P., "Numerical/Experimental Study of a Wingtip Vortex in the Near Field," *AIAA Journal*, Vol. 33., No. 9, September 1995, pp. 1561-1568.
15. Duraisamy, K., and Baeder, J., "High Resolution Wake Capturing Methodology for Hovering Rotors," *Journal of the American Helicopter Society*, Vol. 52, No. 2, April 2007, pp. 110-122.
16. Spalart, P. R., and Shur, M., "On the Sensitization of Turbulence Models to Rotation and Curvature," *Aerospace Sciences and Technology*, Vol. 1, No. 5, July 1997, pp. 297-302.
17. Nichols, R. H., "Algorithm and Turbulence Model Requirements for Simulating Vortical Flows," AIAA 2008-0337, AIAA 46th Aerospace Sciences Meeting and Exhibit, Reno, NV, January 2008.
18. Potsdam, M. A., and Strawn, R. C., "CFD Simulations of Tiltrotor Configurations in Hover," *Journal of the American Helicopter Society*, Vol. 50, No. 1, January 2005, pp. 82-94.
19. Dimanlig, A. C. B., Meadowcroft, E. T., Strawn, R., and Potsdam, M., "Computational Modeling of the CH-47 Helicopter in Hover," American Helicopter Society 62nd Annual Forum, Virginia Beach, VA, May 2007.
20. Buning, P. G., Gomez, R. J., and Scallion, W. I., "CFD Approaches for Simulation of Wing-Body Stage Separation," AIAA 2004-4838, AIAA 22nd Applied Aerodynamics Conference, Providence, RI, August 2004.
21. Buning, P., "Consolidation of Time-Accurate, Moving Body Capabilities in OVERFLOW", 6th Overset Composite Grid and Solution Technology Symposium, Ft. Walton Beach, FL, October 2002.
22. Chan, W. M., Meakin, R. L., and Potsdam, M. A., "CHSSI Software for Geometrically Complex Unsteady Aerodynamic Applications," AIAA 2001-0593, AIAA 39th Aerospace Sciences Meeting and Exhibit, Reno, NV, January 2001.
23. Strawn, R. C., and Djomehri, M. J., "Computational Modeling of Hovering Rotor and Wake Aerodynamics," *AIAA Journal of Aircraft*, Vol. 39, No. 5, September-October 2002, pp. 786-793.
24. Young, L. A., Booth Jr., E. R., Yamauchi, G. K., Botha, G., and Dawson, S., "Overview of the Testing of a Small-Scale Proprotor," American Helicopter Society 55th Annual Forum, Montreal, Canada, May 1999.
25. Swanson, S. M., McCluer, M. S., Yamauchi, G. K., and Swanson, A. A., "Airloads Measurements from a 1/4-Scale Tiltrotor Wind Tunnel Test," 25th European Rotorcraft Forum, Rome, Italy, September 1999.
26. Johnson, W., "Calculation of Tilt Rotor Aeroacoustic Model (TRAM DNW) Performance, Airloads, and Structural Loads," American Helicopter Society Aeromechanics Specialists' Meeting, Atlanta, GA, November 2000.

27. Kufeld, R. M., Balough, D. L., Cross, J. L., Studebaker, K. F., Jennison, C. D., and Bousman, W. G., "Flight Testing of the UH-60A Airloads Aircraft," American Helicopter Society 50th Annual Forum, Washington, D.C., May 1994.
28. Bousman, W. G., and Kufeld, R. M., "UH-60A Airloads Catalog," NASA TM-2005-212827, August 2005.
29. Potsdam, M. A., Yeo, H., and Johnson, W., "Rotor Airloads Prediction Using Loose Aerodynamic/Structural Coupling," American Helicopter Society 60th Annual Forum, Baltimore, MD, June 2004.
30. Bousman, W. G., "A Qualitative Examination of Dynamic Stall from Flight Test Data," American Helicopter Society 53rd Annual Forum, Virginia Beach, VA, April 1997.
31. Datta, A., and Chopra, I., "Prediction of UH-60A Dynamic Stall Loads in High Altitude Level Flight using CFD/CSD Coupling," American Helicopter Society 61st Annual Forum, Grapevine, TX, June 2005.
32. <http://www.chinook-helicopter.com/standards/areas/blade.html>

	TRAM	CH-47 [32]	UH-60A
description	0.25-scale V-22 rotor	Full-scale	Full-scale
rotor radius	57.0 in.	30 ft.	26.83 ft.
solidity, σ	0.105	0.0849	0.0826
chord	5.5 in. (tip)	32.0 in.	20.76 in.
twist	-38 deg, nonlinear	-12 deg	-16 deg nonlinear

Table 1. Rotor physical characteristics.

	TRAM	CH-47 [32]	UH-60A
hover tip Mach number	0.62	0.633	0.666
advance ratio, μ	0.0	0.0	0.24
Re (million)	2.1 (tip)	12.0	4.6
C_T/σ	0.143	-	0.129
collective	14 deg	8 - 12 deg	~14 deg

Table 2. Nominal test conditions.

turbulence model		formulation	C_T	C_Q	FM
DNW	test	-	0.01493	0.001653	0.780
BB	baseline	steady	0.01464	0.001678	0.728
BB	laminar off-body	steady	0.01461	0.001668	0.749
BB	freestream off-body	steady	0.01455	0.001650	0.752
BB	laminar off-body	unsteady	0.01481	0.001672	0.762
SA	baseline	steady	0.01477	0.001683	0.753
SA	laminar off-body	steady	0.01478	0.001678	0.757
SA	DM	steady	0.01481	0.001683	0.757
SA	baseline	unsteady	0.01514	0.001708	0.771
SA	laminar off-body	unsteady	0.01514	0.001702	0.774
SA	DM	unsteady	0.01515	0.001714	0.774
SADES	baseline	unsteady	0.01514	0.001703	0.773

Table 3. Calculated TRAM hover performance, 14-deg collective.

			CFD collective (deg)		
	near-body spatial	formulation	8	10	12
baseline [19]	O(2)	unsteady	-0.069	-0.056	-0.060
laminar off-body	O(4)	unsteady	-0.007	+0.004	+0.007
laminar off-body	O(4)	steady		-.037	

Table 4. Calculated CH-47 isolated rotor hover figure of merit compared with experimental test data, $FM_{CFD}-FM_{TEST}$.

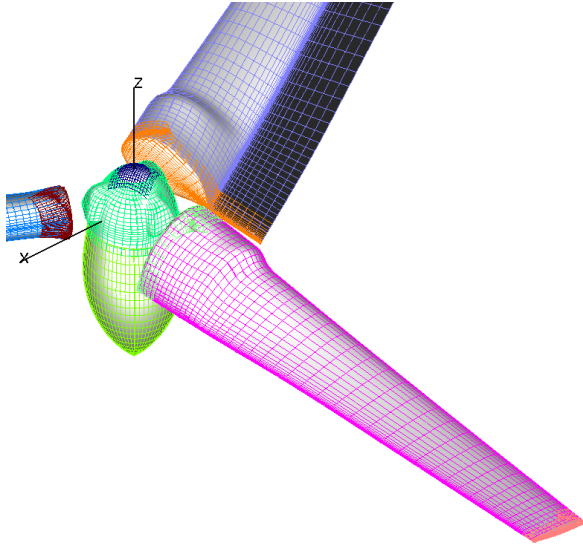


Figure 1. Isolated TRAM rotor geometry and baseline surface grids (every other point).

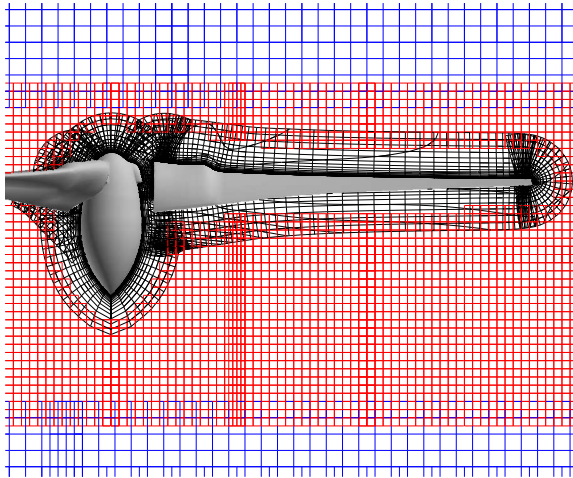


Figure 2. Slice through isolated TRAM rotor volume grids (every other point). black – near-body, red – finest level off-body, blue – coarser level off-body.

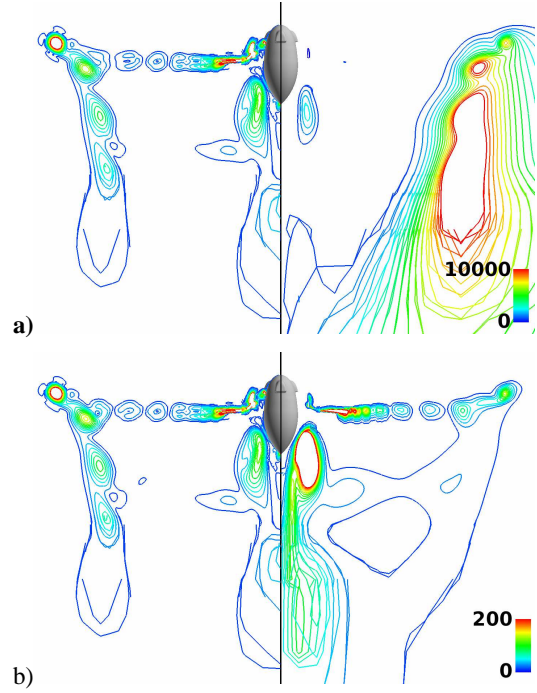


Figure 3. TRAM vorticity (left) and eddy viscosity (right) contours for Baldwin-Barth a) baseline and b) laminar off-body, 30-deg wake age. Note μ_T scale change.

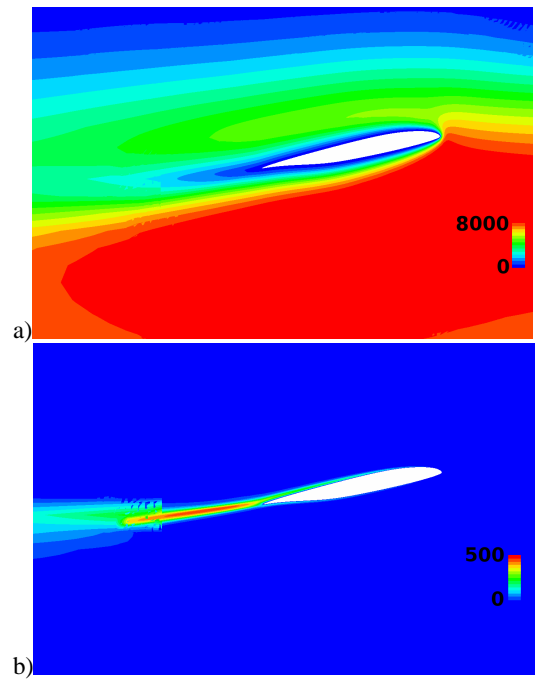


Figure 4. TRAM eddy viscosity contours for Baldwin-Barth a) baseline and b) laminar off-body, 90% span. Note μ_T scale change.

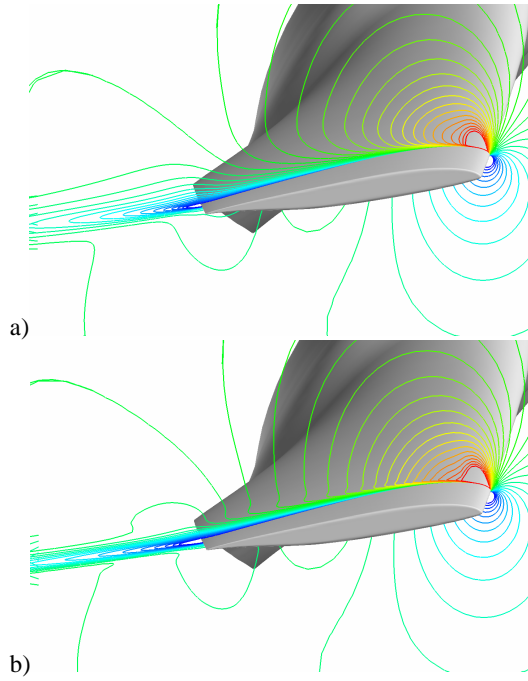


Figure 5. TRAM relative velocity magnitude contours for Baldwin-Barth a) baseline and b) laminar off-body, 90% span (blue – low, red – high).

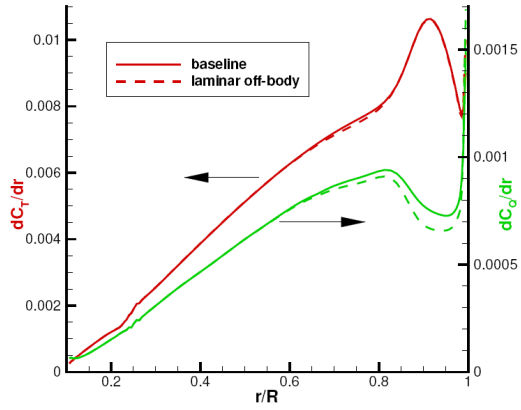


Figure 6. TRAM rotor thrust and torque span loading.

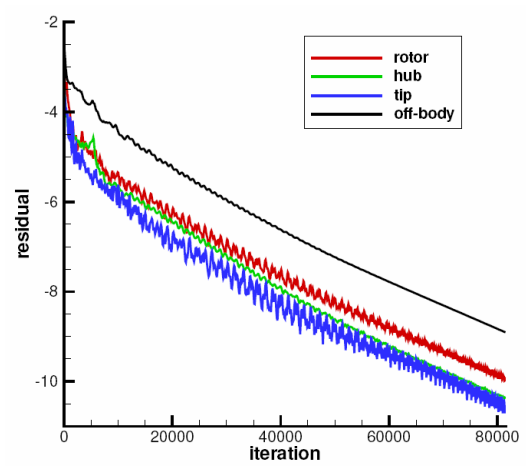


Figure 7. TRAM rotor steady-state hover residual convergence for near-body and off-body grids, Baldwin-Barth laminar off-body.

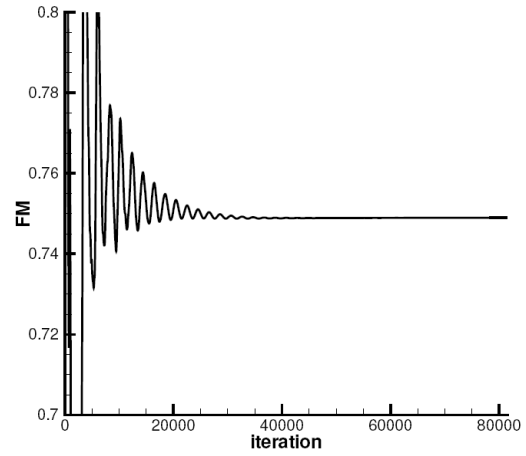


Figure 8. TRAM rotor steady-state hover figure of merit convergence, Baldwin-Barth laminar off-body.

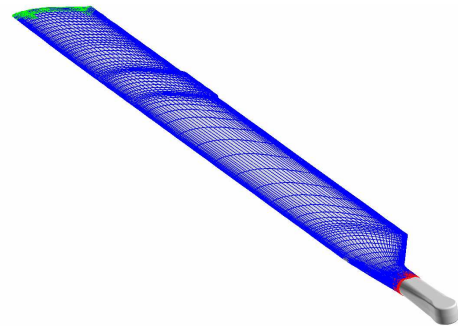


Figure 9. CH-47 rotor blade overset surface grid [19].

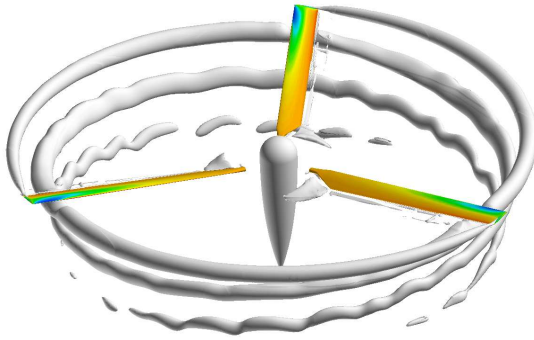


Figure 10. CH-47 computed rotor surface pressure contours and wake geometry (Q criteria) for isolated hovering rotor.

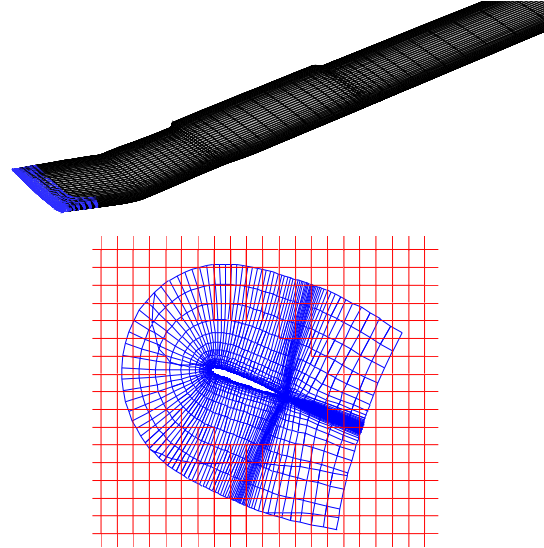


Figure 13. UH-60A configuration coarse surface and volume grids.

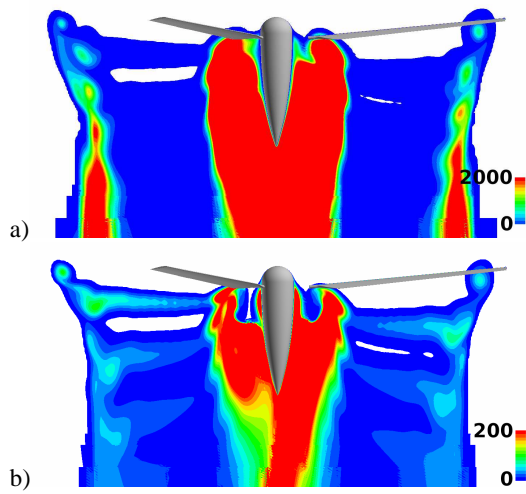


Figure 11. CH-47 eddy viscosity contours for Spalart-Allmaras a) baseline and b) laminar off-body, 0 deg wake age. Note μ_T scale change.

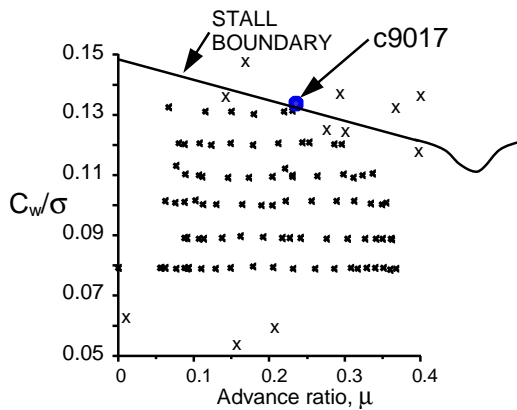


Figure 12. UH-60A Airloads test points and stall boundary.

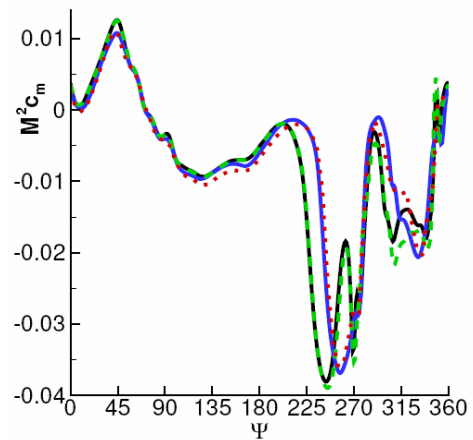
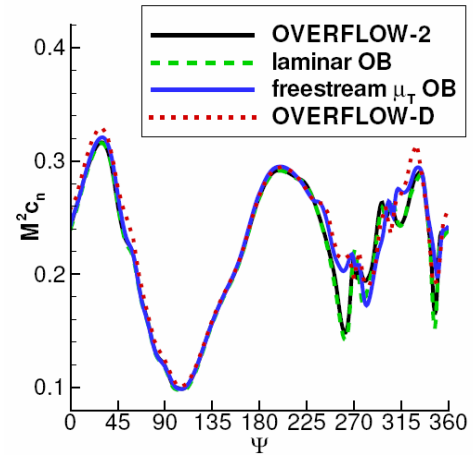


Figure 14. UH-60A airloads (normal force and pitching moment) for various off-body grid Baldwin-Barth turbulence model options, 86.5% span, c9017 conditions.

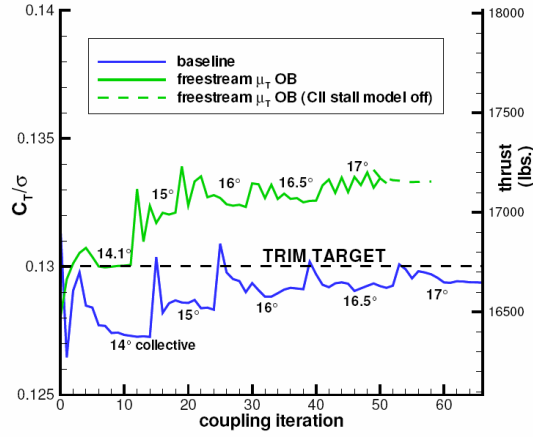


Figure 15. UH-60A OVERFLOW-2/CAMRAD II trimmed collective sweep, c9017 conditions.

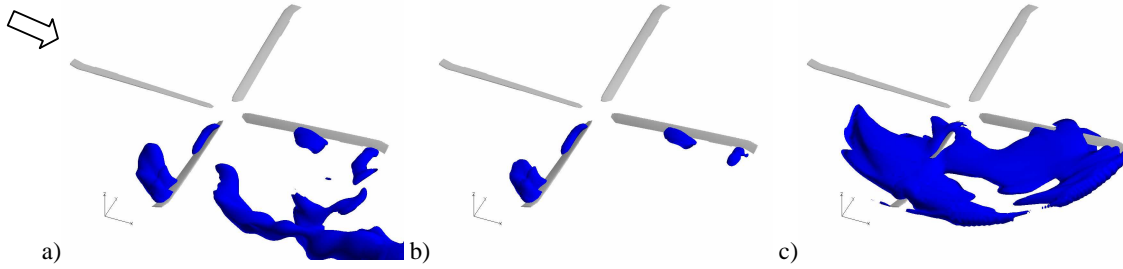


Figure 16. UH-60A eddy viscosity iso-surfaces for Baldwin-Barth a) baseline, b) laminar off-body, and c) freestream off-body eddy viscosity, c9017 conditions (flow is left to right).

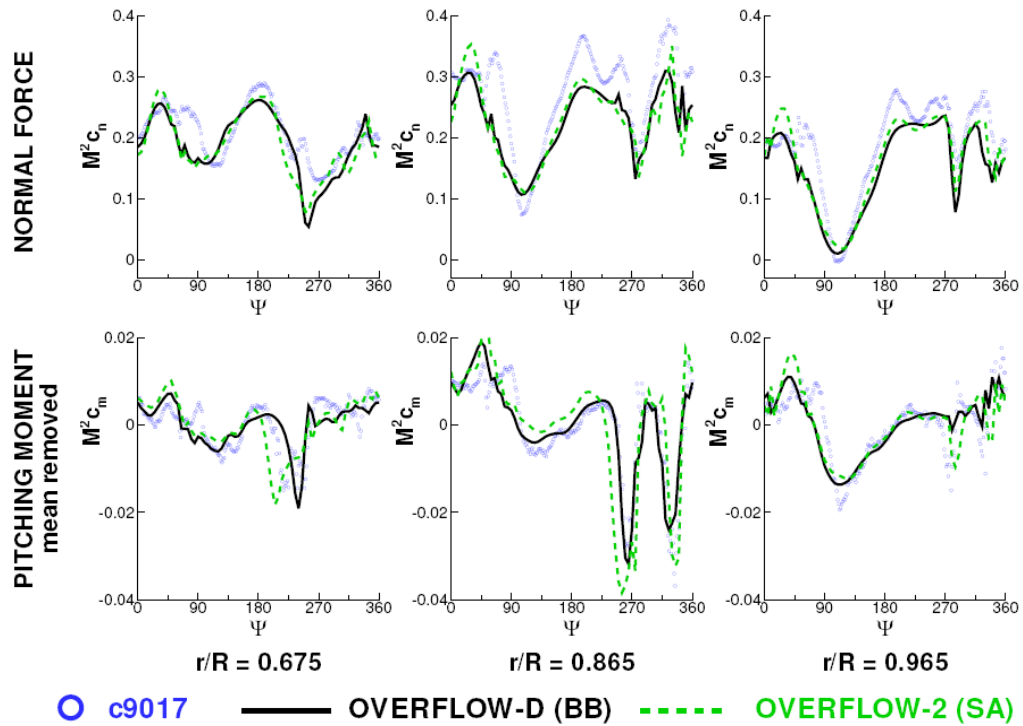


Figure 17. UH-60A airloads (normal force and pitching moment) using OVERFLOW/CAMRAD coupling, c9017 conditions.